Cryosectioning-enabled super-resolution microscopy for studying nuclear architecture at the single protein level

Johannes Stein[1,2,*], Maria Ericsson[3], Michel Nofal[1], Lorenzo Magni[1], Sarah Aufmkolk[2], Ryan B. McMillan[1], Laura Breimann[2], Conor P. Herlihy[2], S. Dean Lee[2], Andréa Willemin[4,5], Jens Wohlmann[6], Laura Arguedas-Jimenez[4], Peng Yin[1], Ana Pombo[4,5], George M. Church[1,2,*] and Chao-ting Wu[2,*]

[1] Wyss Institute of Biologically Inspired Engineering, Boston, MA, USA.

[2] Department of Genetics, Harvard Medical School, Boston, MA, USA.

[3] Blavatnik Institute, Harvard Medical School, Boston, MA, USA.

[4] Max-Delbrück-Center for Molecular Medicine in the Helmholtz Association (MDC), Berlin Institute for Medical Systems Biology (BIMSB), Epigenetic Regulation and Chromatin Architecture Group, Berlin, Germany.

[5] Humboldt-Universität zu Berlin, Institute for Biology, Berlin, Germany.

[6] Department of Biosciences, University of Oslo, Norway.

*Corresponding authors. Contact: johannes.stein@wyss.harvard.edu (J.S.), gchurch@genetics.med.harvard.edu (G.M.C.), twu@genetics.med.harvard.edu (C.-t.W.)

Abstract

DNA-PAINT combined with total Internal Reflection Fluorescence (TIRF) microscopy enables the highest localization precisions, down to single nanometers in thin biological samples, due to TIRF's unique method for optical sectioning and attaining high contrast. However, most cellular targets elude the accessible TIRF range close to the cover glass and thus require alternative imaging conditions, affecting resolution and image quality. Here, we address this limitation by applying ultrathin physical cryosectioning in combination with DNA-PAINT. With "tomographic & kinetically-enhanced" DNA-PAINT (tokPAINT), we demonstrate the imaging of nuclear proteins with sub-3 nanometer localization precision, advancing the quantitative study of nuclear organization within fixed cells and mouse tissues at the level of single antibodies. We believe that ultrathin sectioning combined with the versatility and multiplexing capabilities of DNA-PAINT will be a powerful addition to the toolbox of quantitative DNA-based super-resolution microscopy in intracellular structural analyses of proteins, RNA and DNA *in situ*.

Introduction

Super-resolution microscopy provides visual access down to the nanoscale of biological specimens[1–6], with Single-Molecule Localization Microscopy (SMLM) routinely enabling sub-20 nm resolution by recording stochastic fluorescence events to obtain localizations from individual fluorescent molecules[7]. One form of SMLM, Points Accumulation for Imaging in Nanoscale Topography[4] (PAINT), elegantly achieves such stochastic single molecule blinking by the transient binding of otherwise diffusing fluorescent probes to targets of interest. A powerful implementation of PAINT, called DNA-PAINT[8,9], leverages fluorescently-labeled 'imager' strands transiently binding to their complementary 'docking' strands attached to the target molecules. Besides enabling cellular imaging at sub-10 nanometer resolution[10], the programmability of DNA-mediated binding enables molecular counting[11,12] as well as multiplexing via sequential imaging of multiple targets labeled with orthogonal docking strand sequences[13].

An important experimental factor in DNA-PAINT, and SMLM in general, is the physical size of the imaging volume from which single-molecule blinking is recorded, as additional volume increases noise. A convenient way of reducing the imaging volume is through optical sectioning[7,9,14], which enhances the signal-to-noise ratio for single-molecule detection and, hence, the achievable resolution[15]. Among optical sectioning approaches, total internal reflection fluorescence[7,16] (TIRF) microscopy enables the smallest imaging volume, down to <200 nm above the cover glass, and, in the context of cellular DNA-PAINT imaging, has enabled the highest achieved resolutions to date[10,17]. Cellular targets further from the cover glass, however, become inaccessible to TIRF and, thus, require alternative microscope modalities[14,18–20]. One such modality is highly inclined laminated optical sheet (HILO) microscopy[21], which can accommodate larger volumes and thus enable researchers to reach deeper in into samples, however, at a compromised resolution[9,22]. Furthermore, for dense targets being imaged with DNA-PAINT, a larger imaging volume can limit imager binding rates at the single docking strand level, as imager concentrations need to be reduced to ensure sparse, non-overlapping blinking[7,9].

Physical sectioning is an alternative approach that has been explored for SMLM[2,23–25] and DNA-PAINT in tissues[26,27], as it enables any cellular region captured in a section to be imaged under ideal TIRF conditions[2]. Furthermore, sectioned samples offer the additional advantage of being more accessible to the imaging buffer and, thus, binding of imager strands. The perpetual nature of repeated imager binding at controllable rates is a hallmark of DNA-PAINT and has led to a diverse range of quantitative *in vitro*[12,28–31] and *in situ*[11,28] applications, such as the counting of target molecules within fixed cells and tissues via qPAINT[11]. A physically-sectioned sample that is openly accessible to the imaging solution could potentially exhibit improved binding kinetics, thus elevating our ability to leverage DNA-PAINT as a quantitative tool.

Here, we adopt the Tokuyasu-method[32], a cryosectioning approach widely known from immunogold electron microscopy and for its excellent antigenicity[33], to explore the potential of physical sectioning for intranuclear DNA-PAINT imaging (**Fig. 1**a). Making the nucleus – a dense and challenging imaging environment[34] – accessible for TIRF-based, quantitative DNA-PAINT would provide a promising path for studying nuclear architecture and the intricate interplay between genome organization and function at the molecular level[35,36]. Furthermore, established fluorescence microscopy protocols for studying nuclear targets, such as RNA polymerase II (Pol II), within ultrathin Tokuyasu sections (~150 nm)[37–39] served as an ideal starting point for exploring their potential for intranuclear DNA-PAINT. With "tomographic & kinetically-enhanced" DNA-PAINT or "tokPAINT", we demonstrate nuclear imaging of Pol II at ~3 nm localization precision. With super-resolution microscopy enabling resolutions down to the level of single proteins[10,40–44], we tested tokPAINT's capacity in this regard and achieved, to the best of our knowledge, the first time in which a highly abundant antigen, such as Pol II, is detected at the level of single antibodies across an entire nuclear field by means of fluorescence microscopy. Furthermore, we show that the accessibility of ultrathin cryosections enhances imager binding kinetics, minimizing contributions of non-specific localizations[45] and promoting molecular counting via qPAINT[11]. We also demonstrate multiplexed tokPAINT imaging via Exchange-PAINT[13], the latter having been previously demonstrated for thicker tissue cryosections[26,27]. Enabling simultaneous nanoscale interrogations of proteins, nucleic acids and combinations thereof, as well as astigmatism-based imaging in 3D, we believe tokPAINT will become a powerful addition for studying nuclear organization with DNA-PAINT[34,46–49].

Results

tokPAINT enables TIRF-based nuclear DNA-PAINT imaging with enhanced resolution and binding kinetics

To assess the potential of nuclear tokPAINT imaging in intact cells, we chose to target the largest subunit of Pol II, Rpb1, as a highly abundant nuclear protein (**Fig. 1**b). We focused, in particular, on its C-terminal domain (CTD), which features 52 heptad repeats of the consensus motif YSPTSPS, the residues of which are posttranslationally modified during the transcription cycle and are also involved in promoting co-transcriptional RNA splicing[50]. Using a primary antibody directed against hyperphosphorylated Serine-5 of the CTD (S5p), we then leveraged previously optimized protocols for diffraction-limited imaging within ultrathin cryosections (~150 nm) under ultrastructure-preserving conditions within the nucleus[38] (**Supplementary Fig. 1**). If not stated otherwise, we refer to ultrathin cryosections of ~150 nm thickness as 'cryosections', which were exclusively used for all tokPAINT experiments and controls presented in this work.

We labeled fixed intact HeLa cells as well as cryosections of fixed HeLa cells with both primary antibodies and oligo-conjugated secondary antibodies designed for 2D DNA-PAINT imaging (**Methods**). Intact cells were then imaged using DNA-PAINT with HILO illumination, while cryosections were imaged via tokPAINT using TIRF illumination at a TIRF angle that ensured approximately homogeneous intensity over the section thickness[51]. Duration of data acquisition was kept identical for both HILO DNA-PAINT and tokPAINT imaging, and imager concentrations were adjusted individually to ensure sparse blinking in each experiment (**Methods**). **Figures 1**c and **1**d depict the reconstructed super-resolution images obtained via HILO DNA-PAINT and tokPAINT, respectively. Despite similar densities measured per nuclear area (~570 localizations/μm^2 for HILO DNA-PAINT, ~620 localizations/μm^2 for tokPAINT; **Supplementary Fig. 2**), localizations appeared less clustered and more widely distributed in the HILO DNA-PAINT image presumably due to the larger imaging volume and lower resolution (**Supplementary Fig. 3**). TIRF illumination in tokPAINT led to a 7×-higher signal-to-noise ratio, as compared to HILO (~72 vs. ~10, respectively; **Supplementary Fig. 3**), translating to an almost 3-fold improvement in localization precision, down to ~3 nm as compared to ~8.3 nm in HILO DNA-PAINT (determined via Nearest Neighbor Analysis[52], NeNA); **Fig. 1**c and d, respectively). As a reference, we performed *in vitro* DNA-PAINT imaging of surface-immobilized DNA origami[53] structures that featured a docking strand pattern with 20 nm spacing[9] using TIRF. This resulted in a localization precision of 2.8 nm (**Extended Data Fig. 1**), demonstrating that tokPAINT can translate the resolution achievable with TIRF under *in vitro* conditions to the nuclei of fixed cells.

We next asked to what extent the small sample volume and its open accessibility to the imaging solution improved imager binding statistics for nuclear tokPAINT imaging as compared to that for HILO DNA-PAINT, where imagers must first diffuse through the cellular matrix before reaching the focal plane in the nucleus. In fact, inspecting individual localization clusters in both data sets indicated significantly higher imager binding frequencies as well as number of localizations with tokPAINT as compared to HILO DNA-PAINT (yellow circles and insets, **Fig. 1**c and d, respectively). To test this observation, we performed

a spatiotemporal clustering analysis, as described in detail in **Supplementary Figure 4**. In the first step, we applied the clustering algorithm DBSCAN[54] to each data set in order to identify local accumulations of localizations as localization clusters. Subsequently, we excluded localization clusters that were devoid of repeated imager binding and that, hence, presumably resulted from non-specific sticking of imagers[17,28,55]. Remarkably, ~60 % of all nuclear localizations in the tokPAINT data set could be assigned to a localization cluster with repeated binding in contrast to only ~18 % in the case of HILO DNA-PAINT (**Supplementary Fig. 5**), implying that a large fraction of tokPAINT data is amenable to downstream quantitative analysis.

We note that, due to the high abundance of Pol II within the nucleus, the larger imaging volume of HILO DNA-PAINT required our data acquisition to be performed at low imager concentrations to prevent overlapping blinking. Sufficient binding statistics can be achieved by extending the duration of image acquisition for nuclear DNA-PAINT in intact cells using HILO illumination[46–48]. Furthermore, use of fluorogenic imagers[19] could enhance both achievable resolution through background reduction and binding statistics by preventing bleaching of diffusing imagers[56] (also see note in **Supplementary Fig. 4**).
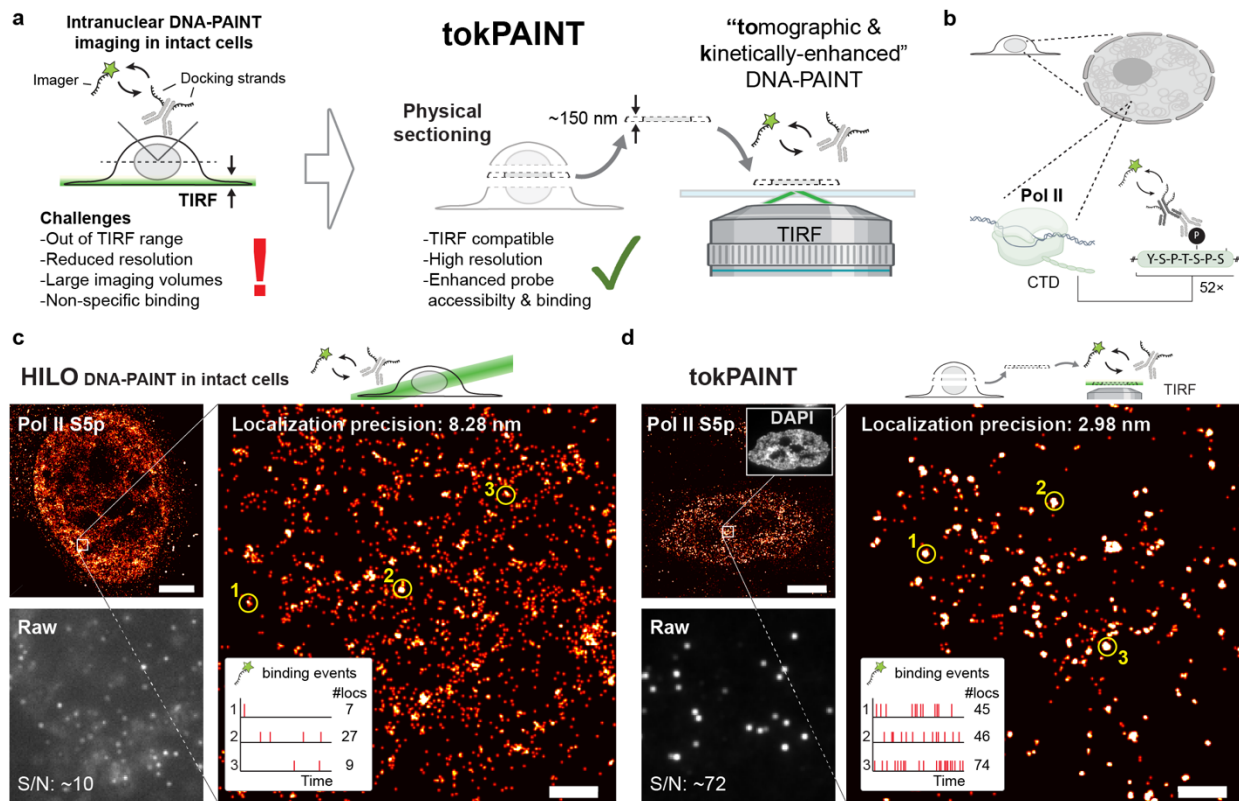

Figure 1 | tokPAINT enables TIRF-based DNA-PAINT imaging of intranuclear targets. a tokPAINT schematic. Ultrathin cryosectioning enables nuclear DNA-PAINT imaging under TIRF conditions. **b** Immunolabeling of Pol II CTD Serine-5 phosphorylation (S5p) for DNA-PAINT imaging via docking strand-conjugated secondary antibodies. **c** Top left: HILO DNA-PAINT image of Pol II S5p within intact HeLa cell. Bottom left: frame from HILO DNA-PAINT raw data acquisition including signal-to-noise ratio (S/N). Right: magnified region as indicated by white square. Time traces of imager binding and number of localizations are shown for three regions indicated by yellow circles. **d** Top left: tokPAINT image of Pol II S5p. The inset shows the same cell imaged in the DAPI channel. Bottom left: frame from tokPAINT raw data acquisition including S/N ratio. Right: magnified region as indicated by white square. Time traces of imager binding and number of localizations are shown for three regions indicated by yellow circles. Scale bars, 5 μm in (**c,d**), 400 nm in zoom-ins.

tokPAINT enables quantitative nanoscale analysis of nuclear Pol II

The sparse distribution of localization clusters after kinetic filtering in tokPAINT (**Fig. 2**a) was reminiscent of immunogold experiments in which antibodies labeled with gold nanospheres (diameters ~5-15 nm) permit antigens to be detected in cryosections by TEM at the level of single antibodies[33]. To determine whether the resolution possible through tokPAINT would enable single antibodies labeled with docking-strands to be visualized, we performed a range of center-of-mass alignments to obtain averaged sum images for a decreasing minimum number of localizations per cluster (**Supplementary Fig. 6**). We found that localizations in sum images were approximately Gaussian distributed with their standard deviations converging to a minimum. In other words, further reduction of localizations per cluster did not reduce the localization spread. **Figure 2**a displays the convergent sum image with a standard deviation (σ) of 3.4 nm and a full width at half maximum of ~8 nm (FWHM ≈ 2.355×σ), indicating that localizations likely accumulated from individual docking strand-conjugated secondary antibodies, whose physical size ~10 nm[57].

However, repeated imager binding on its own is not necessarily indicative of signal specificity since certain cellular features such as single-stranded RNA could potentially also lead to repeated binding. Furthermore, antibodies could non-specifically bind and thus position docking strands within the sample. To estimate the impact of false positive localization clusters, we performed a set of negative controls under conditions identical to that of previous tokPAINT acquisitions, but on cryosections incubated i) without both primary and secondary antibodies or ii) with secondary antibody only (**Fig. 2**b, top and bottom, respectively, and **Supplementary Fig. 7**). We found a negligible number of false positive localization clusters in both cases as compared to that in tokPAINT experiments labeled with both primary and secondary antibodies (~0.01 loc.-clusters/μm^2 vs. ~6 loc.-clusters/μm^2, respectively; see **Fig. 2**b and **Fig. 2**a). Lastly, we tested the specificity of the primary antibody against Pol II S5p by treating cryosections with phosphatase in order to neutralize phosphorylation sites prior to staining for indirect immunofluorescence[38] (**Fig. 2**c). Reassuringly, this led to a 3-fold reduction in immunofluorescence intensity (**Fig. 2**c).

With indirect labeling, it is likely that the underlying antigen distribution is amplified, since several secondary antibodies can bind per primary antibody. Thus, we next asked whether we could exploit the imager binding kinetics to estimate the number of DNA-conjugated antibodies via qPAINT[11] as well as measure any difference as compared to directly-conjugated primary antibodies. In qPAINT, the average imager binding frequency for the smallest identifiable localization clusters in a data set is taken as a reference (**Fig. 2**d). Assuming the reference represents single antibodies, a localization cluster with N antibodies would have an N-times higher binding frequency[11]. **Figure 2**e displays counting results obtained from four independent experiments, two performed using indirect staining (primary antibodies + docking strand-conjugated secondary antibodies) and two performed using direct staining (docking-strand conjugated primary antibodies). The N distributions were in close agreement, with a median N of ~2 antibodies per localization cluster. The consistency of counting results between both labeling approaches indicated that any signal amplification caused by multiple secondary antibodies binding to each primary antibody was likely to be roughly uniform across all primary antibodies and did not confound relative

counting statistics. As docking strands can suffer from photo-induced damage for extended DNA-PAINT acquisitions[58] and affect molecular counting results[58], we repeated quantitative tokPAINT imaging for a 3x longer image acquisition time, validating that docking strand depletion had negligible effects on our results (**Supplementary Fig. 8**).

Based on these results, we estimate ~200,000-300,000 Pol II S5p antibodies per HeLa cell, which aligns with earlier estimates of ~65,000 engaged Pol II[59] and ~320,000 copies of Rpb1[60] per HeLa cell. Our data also enabled us to assess the spatial distribution of Pol II S5p, which is known to associate with active chromatin or nuclear compartments, such as transcription factories and nuclear speckles[50]. Such nuclear regions correlate with low intensities when stained for DNA using DAPI (4',6-diamidino-2-phenylindole). As expected, we observed both higher antibody-per-cluster counts (**Fig. 2**e) and a higher overall cluster density as determined by nearest neighbor distance analysis[61] for these regions (**Extended Data Fig. 2**).

Note that the accuracy of molecular counting could be improved via smaller affinity labels, such as nanobodies[62] or genetic tags[63]. Smaller labels could reduce the 'linkage error', which causes localizations to be displaced away from the true epitope position by the physical size of the label, as well as mitigate the reduction of epitope accessibility due to steric hinderance. Genetic tags may also provide a more robust relation between tokPAINT localizations and any underlying molecular distribution by enabling stoichiometric labeling of one docking strand per target protein.
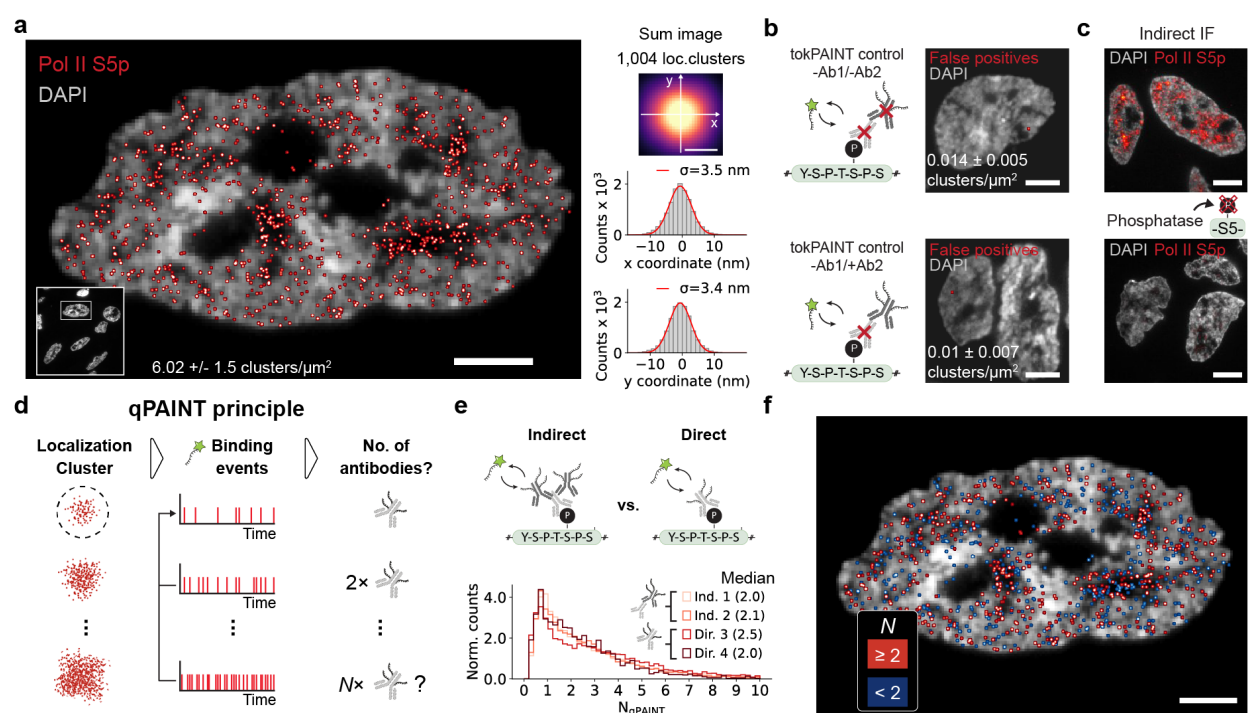

Figure 2 | Quantitative nanoscale analysis of nuclear Pol II distributions via tokPAINT. a tokPAINT Pol II S5p image after removal of localization clusters without repeated imager binding. Right: sum image of 1,004 smallest identifiable localization clusters. The histograms below show the distribution of localizations along the x and y axis (white arrows) and standard deviation obtained by a Gaussian fit (red curve). **b** Top: tokPAINT control imaging of sample processed with the standard labeling protocol but leaving out both primary and secondary antibodies. Bottom: tokPAINT control imaging of sample processed with the standard staining protocol but leaving out primary antibody and incubating secondary antibodies only. Mean and standard deviation of number of false positive localization clusters per nuclear area are given for both controls. **c** Top: Diffraction-limited indirect immunofluorescence image of cryosections labeled for Pol II S5p (red) and DAPI (white). Bottom: same as top, but cryosections

were treated with phosphatase prior to immunostaining. **d** Schematic of quantitative DNA-PAINT[11] (qPAINT). Denser localization clusters are most likely due to a higher local number of docking strand-labeled antibodies *N*. The smallest identifiable localization clusters within a data set are used as a calibration reference (black dashed circle) from which the average imager binding frequency is determined. Relative counting can be performed by comparing the binding frequency of each individual localization cluster to the reference binding frequency (black arrows). Assuming the reference originated from single antibodies, imager binding traces allow relative counting within a DNA-PAINT data set. Right: Counting results for four independent tokPAINT experiments comparing indirect staining (primary/secondary antibody) vs. direct staining (primary antibody only). **e** tokPAINT image displayed in (a), re-rendered according to qPAINT counting results: red (≥2), blue (<2). Scale bars, 5 μm in (**a,e**), 3 μm in (**b,c**) and 5 nm in sum image in (**a**).

Resolution and kinetic enhancement translate to tokPAINT imaging in mouse tissues

Encouraged by previous applications of DNA-PAINT and even Exchange-PAINT to semi-thin (~350 nm) cryosections of tissues[26,27], we explored the application of tokPAINT to tissue samples. Since the Tokuyasu method enables pinpointing of individual antigens via Immunogold EM in both cell and tissue samples[33], we anticipated that tokPAINT should perform equally well in both cells and tissues. To test this, we prepared cryo-blocks from two mouse tissue types (cerebellum and spleen) following established protocols[64] (**Methods**) and processed cryosections for tokPAINT tissue imaging of Pol II S5p. **Figure 3**a depicts super-resolved tokPAINT images of Pol II S5p within cerebellum and spleen cryosections. We measured only slightly reduced NeNA localization precisions as compared to HeLa sections (~4.5 nm vs. ~3 nm, respectively). Analogously to previous HeLa tokPAINT data, we performed a range of center-of-mass alignments to obtain averaged sum images, with decreasing minimum number of localizations per cluster to find the converging distribution width (**Supplementary Fig. 9**), indicating a slight decrease in resolution as compared to that of the HeLa data set, but nevertheless sufficient to detect DNA-conjugated antibodies also within tissue sections (σ ≈4.5 nm and FWHM≈10.6 nm; **Fig. 3**b). As expected, the kinetic enhancement enabled by physical sectioning also translated to tissue imaging: ~50 % of nuclear localizations could be assigned to localization clusters that passed repeated binding criteria, confirming that tissue data sets are also amenable to quantitative analysis. Although nuclei within both tissue types featured, on average, a similar number of localization clusters per cell nucleus, we observed an increased heterogeneity within the spleen as compared to the cerebellum (**Fig. 3**c; 2x standard deviation). This finding, which was confirmed by comparing spatial distributions of nearest neighbor distances and antibody counting (**Fig. 3**d-e), might reflect an intrinsic heterogeneity of nuclear organization in spleen cells and/or a higher number of cell types within the spleen (**Fig. 3**d-e).
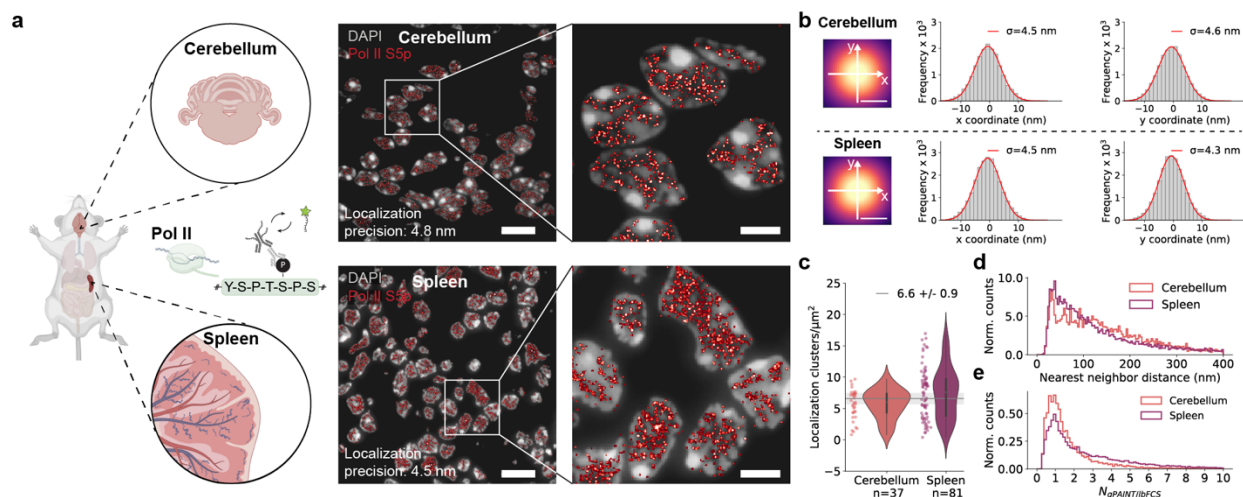
Figure 3 | Resolution and kinetic enhancement translate to tokPAINT tissue imaging. a Tissue blocks of mouse cerebellum and spleen were processed for Tokuyasu sectioning and subsequently stained for Pol II S5p prior to imaging. Top: tokPAINT image of region of mouse cerebellum (NeNA localization precision: 4.8 nm) and zoom-in to white box. Bottom: tokPAINT image of a region of mouse spleen (NeNA localization precision: 4.5 nm) and zoom-in to white box. **b** Comparison of center-of-mass aligned localization clusters for cerebellum and spleen tokPAINT data sets (top and bottom, respectively). The histograms show the distribution of localizations along the x and y axis (white arrows) and give the standard deviation obtained by a Gaussian fit (red curve). **c** Violin plot comparing number of Pol II S5p localization clusters/μm^2 between cerebellum and spleen. Grey line and shaded area show mean and standard deviation, respectively, between both data sets. **d** Nearest-neighbor distance distributions measured in tokPAINT images of mouse cerebellum and spleen. **e** qPAINT distributions measured in tokPAINT images of mouse cerebellum and spleen. Scale bars, 10 μm in (**a**), 3 μm in zoom-ins in (**a**) and 5 nm in (**b**).

Exchange-tokPAINT enables multiplexed nuclear nanoscale imaging

Next, we turned our attention toward several proof-of-concept demonstrations, showcasing the versatility of nuclear tokPAINT imaging with respect to multiplexing. Adapting the Exchange-PAINT principle[13], we conjugated primary antibodies targeting the nuclear lamina (Lamin A/C) and nuclear speckles (SC35[65]), each with an orthogonal docking strand sequence in order to enable multiplexed imaging by sequential exchange of the complementary imager strands for each imaging round (**Fig. 4**a). Exchange-PAINT has the advantage of being free of chromatic aberrations since all imaging rounds can be acquired in the same color channel[13]. **Figure 4**b shows a multiplexed Exchange-tokPAINT image of Lamin A/C, Pol II S5p and SC35, sequentially imaged and subsequently reconstructed using pseudo colors. Not only did sequential imaging enable us to perform quantitative analysis for all three nuclear antigens in parallel, it permitted the spatial probing of intermolecular relationships and features. **Extended Data Fig. 3** provides an overview on how multiplexed tokPAINT data can aid the study of nuclear organization. For example, we observed two peaks in the distribution of nearest neighbor distances for Lamin A/C, which allowed us to separate the signal into a nucleoplasmic and lamina-association fraction[66,67]. Measuring nearest neighbor distances between Pol II S5p and SC35 indicated a spatial organization of Pol II S5p around nuclear speckles with SC35 at their center, as previously observed with TSA-Seq[68].

Beyond multiplexed protein imaging, a potentially even more powerful aspect of cryosections is that the same sections can be subject to both immunostaining and fluorescence in situ hybridization[39,69], enabling analyses of the interplay between targeted proteins and specific sequences of RNA and/or DNA. Here, we performed proof-of-principle tokPAINT imaging of α-tubulin in cryosections that had additionally

been labeled for telomeric repeats via in situ hybridization (**Fig. 4**c). Similarly, hybridization of a poly(dT) probes enabled us to perform tokPAINT imaging of mature mRNA (**Fig. 4**d).
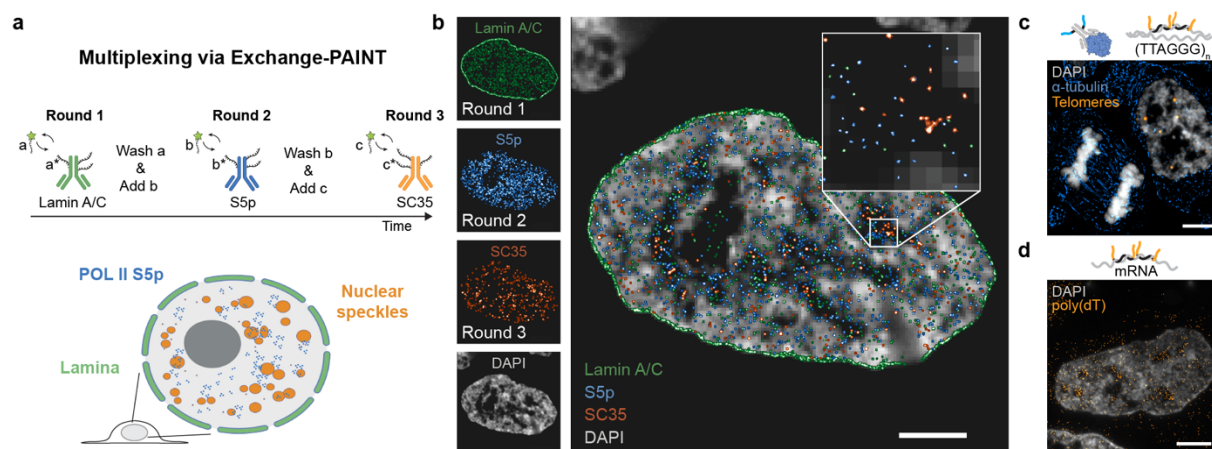

Figure 4 | Exchange-tokPAINT is compatible with multiplexed nuclear nanoscale imaging. a Schematic of Exchange-tokPAINT targeting Lamin A/C, Pol II S5p and SC35. Primary antibodies are conjugated with orthogonal docking strands (sequences *a**, *b** and *c**) and sequentially imaged with imager strands *a*, *b* and *c*. Previous imager is washed out and subsequent imager is added between rounds of imaging. **b** Multiplexed tokPAINT image reconstructed from three rounds of sequential imaging. **c** Combined imaging of protein and DNA using tokPAINT targeting of α-tubulin and telomere repeats via FISH. **d** tokPAINT imaging of mRNA via poly(dT) hybridization probes. Scale bars, 3 μm in (**b**) and 5 μm in (**c,d**).

3D tokPAINT imaging based on astigmatism

tokPAINT data, previously generated through 2D imaging and, thus, resembling a two-dimensional projection of molecules within cryosections, could be significantly enhanced by accessing the axial dimension for a true interrogation of nanoscale organization. To this end, we constructed a simple and affordable (~700$) custom addition to our commercial TIRF system that allowed us to insert a cylindrical lens in front of the camera for astigmatic 3D imaging[70] (**Supplementary Fig. 10**). We first benchmarked our 3D imaging capability, again using surface-immobilized DNA origami with 20-nm docking strand spacing. Although the docking strand arrangement, itself, was in 2D, it nevertheless allowed us to determine the achievable axial resolution in z as well as assess whether astigmatism would significantly reduce our lateral resolution. **Figure 5**a shows an averaged 3D DNA-PAINT sum image of (~450 origami), demonstrating that individual docking strands could be laterally visualized at $FWHM_{x,y} \approx 8.5$ nm ($\sigma_{x,y} \approx 3.6$ nm), which was sufficient to resolve the 20-nm-spaced pattern (**Fig. 5**b). During the origami experiments, we observed that glass slides could be tilted with respect to the optical axis, as revealed when we colored localizations according to their axial position (**Fig. 5**b). To account for this tilt, we performed a z-correction by fitting and subtracting a 2D plane[71] (**Fig. 5**b and **Supplementary Fig. 11**). Post tilt-correction, 3D DNA-PAINT imaging of DNA origami yielded an axial distribution of localizations at $FWHM_z \approx 20$ nm ($\sigma_z \approx 8.5$ nm), in line with the known ~2× axial resolution drop for astigmatic 3D SMLM[70]. An axial resolution of 20 nm would nevertheless allow us to determine distinct axial positions of antibodies within cryosections with a thickness of ~150 nm.

These validations enabled us to move on to 3D tokPAINT imaging within cryosections of fixed HeLa cells, repeating sequential imaging of Lamin A/C, Pol II S5p and SC35 (**Fig. 5**c). The left image in **Figure 5**c

shows the super-resolved Pol II S5p image rendered with a range of colors according to the z-position of each localization over an axial range of 150 nm. It has been shown that, for unpermeabilized cryosections, antibody labeling happens predominantly at both surfaces of sections[72]. However, the permeabilization step in our protocol ensured antibody penetration throughout the sections, as seen for both localization clusters of all colors in the Pol II S5p image alone and the x-z projection of the multicolor Exchange-tokPAINT image (**Fig. 5**c, left and right, respectively). Overall, our 3D tokPAINT results are in close agreement with the cryotome setting for a cutting thickness of 150 nm. Measuring the overall z-distributions, we observed that while Lamin A/C and Pol II S5p labeling penetrated more homogeneously, SC35 exhibited stronger staining toward the top half of the section (**Supplementary Fig. 12**). This result reinforces the additional benefit of using smaller labels such as nanobodies in the future.
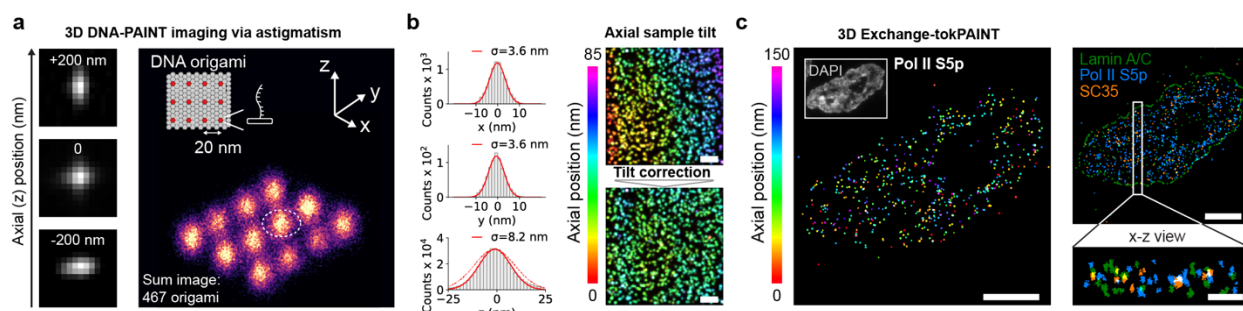

Figure 5 | Astigmatism-based 3D tokPAINT enables axial antibody mapping throughout cryosections. a Validation of cylindrical lens addition to a commercial TIRF system for 3D DNA-PAINT imaging. Left: Astigmatism-based encoding of axial position by reshaping the point spread function. Right: Sum DNA-PAINT 467 DNA origami with 20 nm docking strand pattern. **b** Left, top and middle: x and y line plot histograms across docking strand position indicated by white dashed circle in (a). Left, bottom: Axial distribution of z coordinates of DNA origami data set. The standard deviation obtained by a Gaussian fit (red curve) is given above the histograms. Right: correction of axial sample tilt affecting measured z-distributions (red dashed curve in c). **c** Left: 3D tokPAINT of Pol II S5p. The color code indicates axial position of antibody signal over a range of 150 nm. Right: 3D Exchange-tokPAINT image of Lamin A/C (green), Pol II S5p (blue) and SC35 (orange). Side view (x-z) of localization clusters projected from white box. Scale bars, 5 μm in (**b**), 3 μm in (**c**) and 150 nm in zoom-in.

Discussion

Here, we explored the advantages of ultrathin cryosectioning for intranuclear DNA-PAINT in an approach we termed tokPAINT. We found two major benefits compared to imaging intact fixed cells: leveraging ideal TIRF conditions without range constraint regarding cellular targets and enhanced sample accessibility for improved imager binding. Applying tokPAINT imaging to highly abundant targets such as Pol II we achieved localization precisions down to ~3 nm, enabling us to quantitatively map antibody signal throughout the nuclei of fixed cells and mouse tissues. The de-crowding effect of ultrathin physical sectioning likely enabled pinpointing of individual antibodies, which to our knowledge has for the first time been achieved with DNA-PAINT across the nuclei of fixed cells[14,46–48] or tissues. Of note, we expect the de-crowding effect of cryosections to be equally valuable for RESI[17], a recent implementation of DNA-PAINT reaching Ångstrom resolution, and for complementary nanoscopy technologies such as MINFLUX[43,73,74], especially with respect to dense target structures. While Tokuyasu cryosectioning has been successfully allowed subcellular localization of individual antigens by means of immunogold EM for decades, multiplexing is practically limited to 2-3 distinguishable gold particle sizes. We showed how the multiplexing capabilities of DNA-PAINT[13] provide a route for straightforward combinatorial targeting of

proteins and nucleic acids within the same sections, with the potential for further advances stemming from recent studies demonstrating up to 30-plexed imaging[42,56]. Astigmatism-based axial encoding[70] granted us access to 3D tokPAINT imaging which, in conjuction with computational approaches[75,76] and isotropic 3D imaging approaches[44,77–79], could also be further improved.

Complementing tokPAINT and its application of TIRF illumination for ultrathin sections is the use of HILO microscopy in conjunction with fluorogenic imagers[19] and/or repetitive sequence designs[45,80] to span the depths of whole cells and tissue samples. For example, cellular targets such as membrane receptors, references standards such as nuclear pore complexes[40] (NPCs), and large genomic regions[49] would all be challenging to image with DNA-PAINT within cryosections, unless coupled with serial sectioning and 3D reconstruction. This has been explored for cryosections[81], but might be challenging to automate. tokPAINT could, however, be applied in conjunction with resins that preserve antigenicity and promote serial processing, e.g., as used in Array Tomography[82]. The wealth of information gained from super-resolution studies that are based on imaging of single nuclear 'optical sections'[46,48,83–85] highlight the strong potential for studying nuclear architecture in single sections alone.

Genome function and organization is highly dynamic, which is why it is important to both understand and minimize potential artifacts induced by slow acting chemical fixations[37,86]. As fluorescence-based resolutions are reaching the molecular level, sample fixation by high-pressure freezing followed by freeze substitution – a gold standard in EM – seems a promising route for capturing molecular organization closer to the *in vivo* state[87,88]. Parallel sample preparation should furthermore enable straightforward implementations of tokPAINT for correlative light and electron microscopy[89–92]. With the rise of expansion microscopy[93], it would be interesting to apply tokPAINT to cryosections of previously expanded samples, which could have advantages, such as increasing epitope accessibility and reducing linkage errors[94], but would require prior validation of preserving cellular integrity at the nanoscale.

Finally, we note that all experiments within this study were performed on a 15-year old standard TIRF microscope, with only those experiments involving 3D imaging demanding a minor custom modification. While cryosectioning requires some skill and practice to avoid artifacts during cutting and sample collection, its basics can be learned within a day of training, and it is a technique commonly offered in electron microscopy facilities. Together with available off-the-shelf reagents, open access software[9], and compatibility with standard inverted microscopes, joint work with EM facilities and experts proficient in sample preparation would provide valuable opportunities to the DNA-PAINT community. Decades of Immunogold EM have brought forward thousands of protocols optimized for targets across all kingdoms of life – each posing an immediate starting point for DNA-PAINT and its ever-growing quantitative capabilities. Along these lines, we believe that the potential of tokPAINT extends far beyond studying nuclear organization and will help drive DNA-PAINT toward becoming a routine tool for biological discovery.
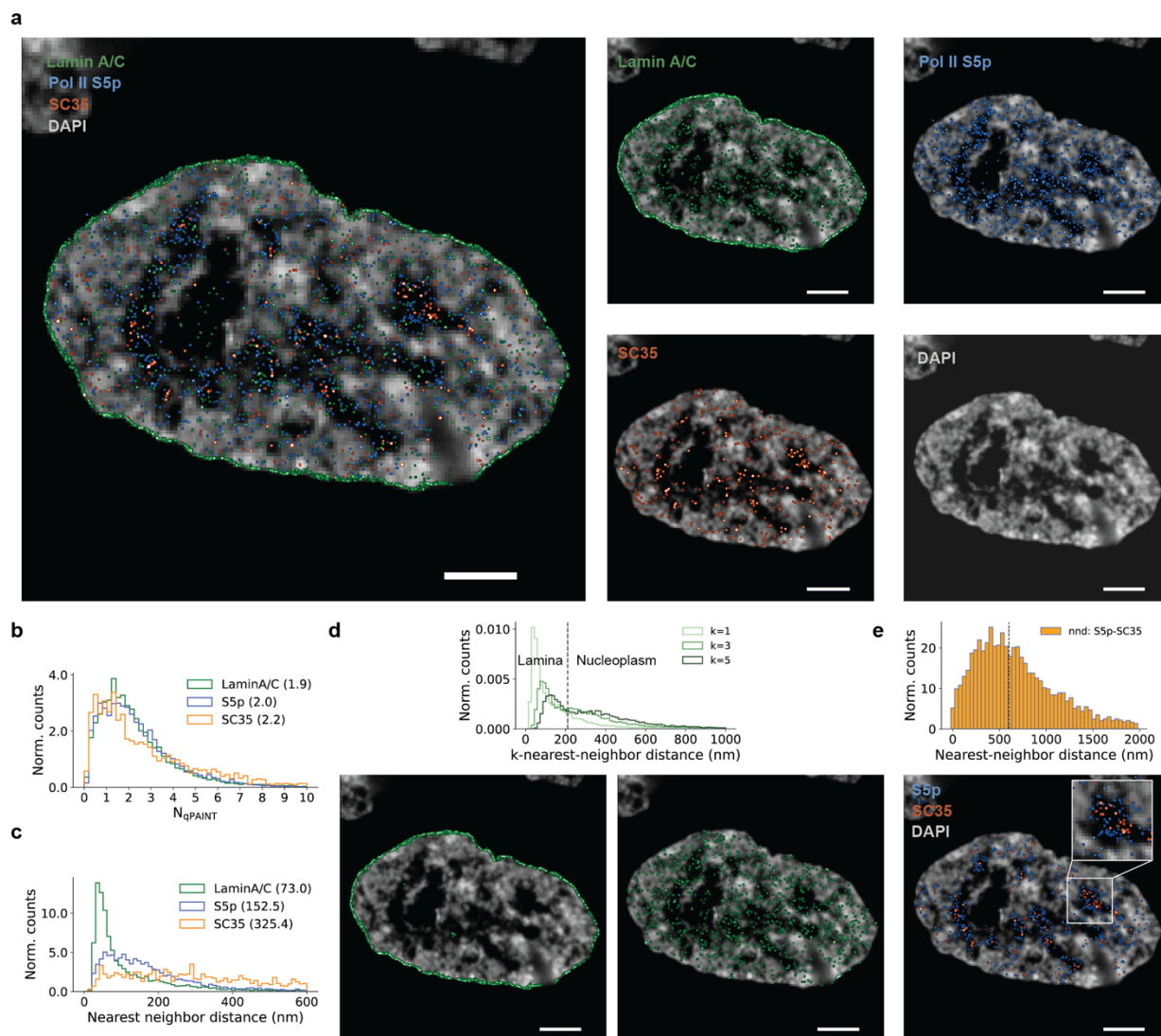
Extended data
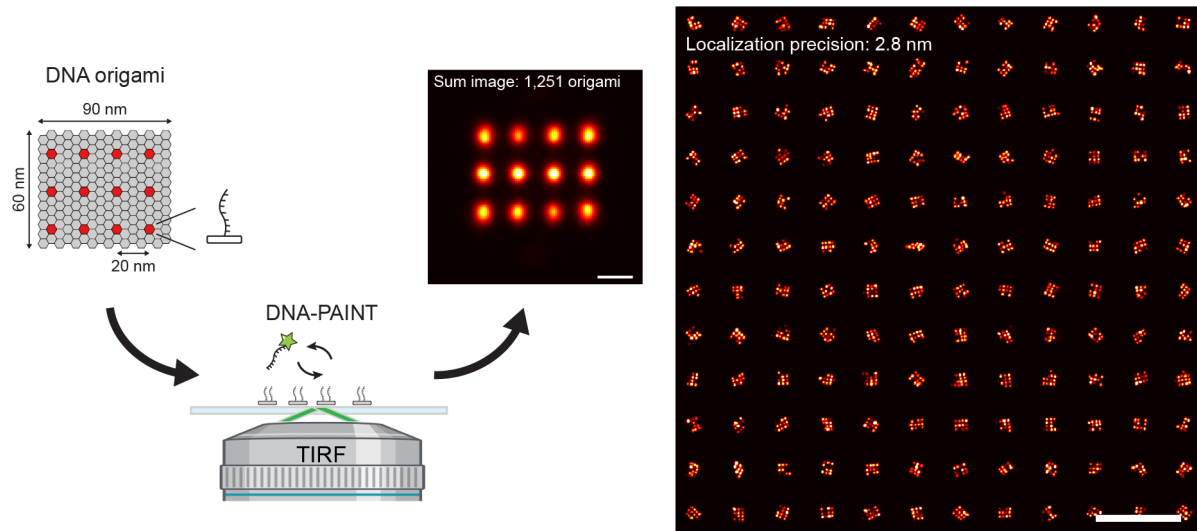
Extended Data Fig. 1 | TIRF-based DNA-PAINT imaging of synthetic DNA origami 20 nm grids. DNA-PAINT image of surface-immobilized DNA origami featuring a pattern of docking strands at 20-nm spacing ('20 nm grids'[9]) acquired on our TIRF system. The left image displays an averaged sum image of 1,251 origami and the right image a random selection of 144 origami arranged in 12x12 square. The localization precision for the data set is stated in the right image. Scale bars, 20 nm in left image and 200 nm in right image.
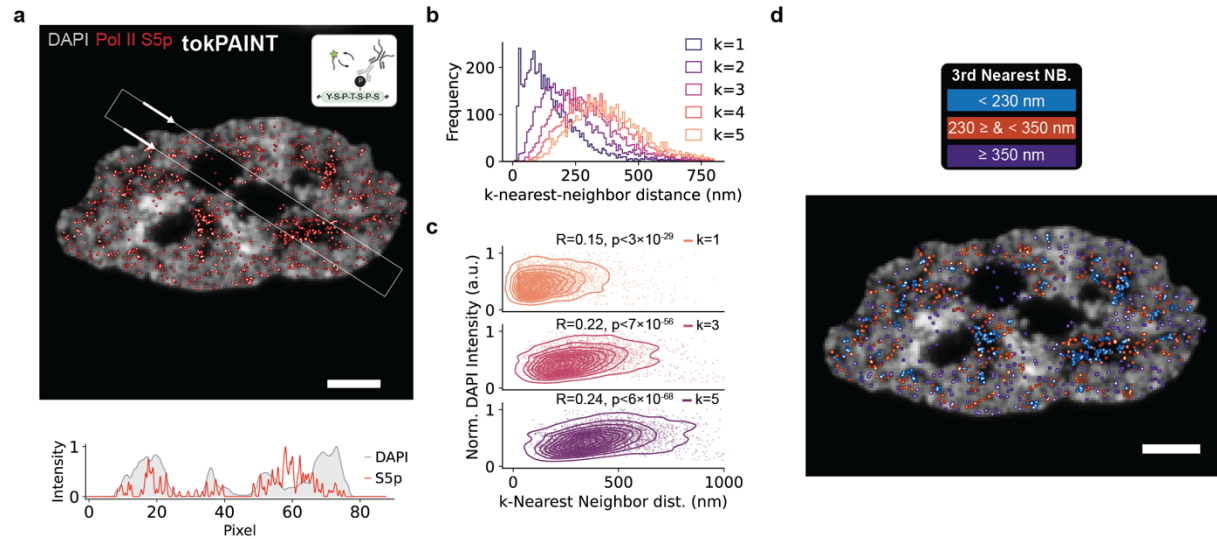
Extended Data Fig. 2 | Pol II S5p correlation analysis DAPI vs. nearest neighbor distances. a. POL II S5p tokPAINT image including DAPI overlay (same as shown in **Fig. 2**a). The line profiles below the image show the POL II S5p and DAPI signal distribution across the white box indicated in the image. The box first crosses two DAPI-negative regions without POL II S5p signal (presumably nucleoli) followed by a third DAPI-negative region featuring high S5p signal. **b** Histogram of k-nearest-neighbor distances between POL II S5p localization clusters. **c** To test the expected anti-correlation between DAPI intensity (as a degree of chromatin compactness) and S5p abundance, which is more associated with open chromatin, we plotted k-nearest neighbor distances (k=1,3,5) vs. normalized DAPI intensity. As expected, localization clusters with small k-nearest neighbor distances, indicating a high local abundance of the antigen, are associated with DAPI weaker regions (k=5, Pearson's R=0.24, p<6x10^{-68}). The weak correlation could be explained by nucleoli counteracting it with DAPI weak regions deprived of S5p. **d** Rendering of the image in a with colors indicating 3rd-nearest-neighbor distance. This visually confirms that DAPI-weak regions tend to feature higher local abundances of POL II S5p localization clusters[37,38]. Scale bars, 3 μm.

Extended Data Fig. 3 | Quantitative analysis of Exchange-tokPAINT: Lamin A/C, Pol II S5p, SC35. a Exchange-tokPAINT image of Lamin A/C, Pol II S5p and SC35 including DAPI image (same as in **Fig. 4**a), overlayed on the left and displayed individually on the right. **b** Histogram of qPAINT counting results obtained for Lamin A/C, Pol II S5p and SC35. **c** Histogram of nearest neighbor distances measured individually for Lamin A/C, Pol II S5p and SC35. **d** Top: inspection of higher order nearest neighbor distance histograms revealed two peaks, indicating the lamina-associated fraction and the nucleoplasmic fraction of Lamin A/C, as confirmed when filtering for each peak (black dashed line) and visualizing the spatial distribution in the images below. **e** Intermolecular nearest neighbor distance measurements between POL II and SC35. Although both antigens are known to associate with nuclear speckles[38], the peak around 500 nm indicates a spatial segregation. Visualization of only Pol II S5p and SC35 localization clusters with a intermolecular distance <600 nm (black dashed line) in fact revealed a more centered organization of SC35 in DAPI-negative regions with S5p in the periphery, which has been similarly observed via genomics-based approaches[68]. Scale bars, 3 μm in (a) and 1 μm in zoom-in.

Online Methods

Materials. Unmodified, dye-labeled, and modified DNA oligonucleotides were purchased from Integrated DNA Technologies, Metabion and Biomers. Unmodified oligos were purified via standard desalting and modified oligos via HPLC. DNA scaffold strands were purchased from Tilibit (p7249, identical to M13mp18). Sample chambers were ordered from Ibidi GmbH (8-well 80827 and 18-well 81817). Tris 1M pH 8.0 (AM9856), EDTA 0.5M pH 8.0 (AM9261), Magnesium 1M (AM9530G) and Sodium Chloride 5M (AM9759) were ordered from Ambion. Streptavidin (S-888) Ultrapure water (15568025), PBS (20012050), 4',6-Diamidino-2-Phenylindole, Dihydrochloride (D1306) (A39255), BSA (AM2616) and TetraSpeck™ Microspheres 0.1 µm (T7279), DMEM (10569) and Dithiothreitol (DTT) were purchased from Thermo Fisher Scientific. BSA-Biotin (A8549), Tween-20 (P9416-50ML), Glycerol (cat. 65516-500ml), (+-)-6-Hydroxy-2,5,7,8-tetra-methylchromane-2-carboxylic acid (Trolox) (238813-5G), methanol (32213-2.5L), 3,4-dihydroxybenzoic acid (PCA) (37580-25G-F), protocatechuate 3,4-dioxygenase pseudomonas (PCD) (P8279-25UN), cell scrapers (CLS353085), Triton-X 100 (93443), Gelatin from cold fish skin (G7041-500G), Formamide (F9037), RNAse A (EN0531), Sodium Azide (S2002), HEPES (H4034-100G), FastAP Alkaline Phosphatase (EF0651), Methyl cellulose 25 CP (M6385-100G), Glycine (G8898), Sodium hydroxide (P3911-1kg), methyl cellulose (M6385), dextran sulfate (D4911) 20xSSC buffer (S6639)and sucrose (S0389) was purchased from Sigma-Aldrich. 10% fetal bovine serum was purchased from Genesee Scientific (25-514). EM grade paraformaldehyde (FA) was purchased from Electron Microscopy Services (15714). 90 nm gold nanoparticles (G-90-20-10 OD10) were purchased from Cytodiagnostics. Primary anti-Lamin A/C antibodies (mouse, 34698) and anti a-tubulin (rabbit, 2125BF) were purchased from Cell Signaling (mouse, 34698). Primary anti-Pol II CTD S5p antibodies (rabbit, ab5131), anti-Digoxigenin (mouse, ab420) and anti-SC35 (mouse, ab11826) were purchased from Abcam. Secondary donkey anti-rabbit labeled with Alexa488 was purchased from Thermo Fisher Scientific (A21206). Secondary donkey anti-rabbit and (711-005-152) and goat anti-mouse (115-005-003) were purchased from Jackson ImmunoResearch Laboratories. 0.5-mL Amino Ultra Centrifugal Filters with 50 kDa molecular weight cutoffs were purchased from Millipore (UFC5050). DBCO-sulfo-NHS ester cross-linker was purchased from Vector Laboratories (CCT-A124). Qubit Protein Assay (Q33211), NuPage 4-12% Bis-Tris protein gels (NP0323BOX), NuPage LDS Sample Buffer (NP0007) was purchased from Invitrogen. InstantBlue Coomassie Protein Stain was purchased from Abcam (ab119211).

Buffers. Four buffers were used for sample preparation and imaging: Buffer A (10 mM Tris-HCl pH 7.5, 100 mM NaCl); Buffer B (5 mM Tris-HCl pH 8.0, 10 mM MgCl2, 1 mM EDTA); Buffer C (1× PBS, 500 mM NaCl); 10x folding buffer (100 mM Tris,10 mM EDTA pH 8.0, 125 mM MgCl2). Buffers were checked for pH. Imaging buffers were supplemented with oxygen scavenging & triplet state quenching system 1× PCA, 1× PCD, 1× Trolox prior to imaging.

PCA, PCD, Trolox. 100× Trolox: 100 mg Trolox, 430 µL 100% Methanol, 345 µL 1 M NaOH in 3.2 mL H2O. 40× PCA: 154 mg PCA was mixed with 10 mL water adjusted to pH 9.0 with NaOH. 100× PCD: 9.3 mg PCD, 13.3 mL of buffer (100 mM Tris-HCl pH 8, 50 mM KCl, 1 mM EDTA, 50% glycerol).

DNA origami design and assembly. DNA origami with 20-nm spaced docking strands ('20 nm grids') were designed previously using the Picasso Design[9] module. A list of all used DNA strands can be found in ref.[95]. Folding of structures was performed using the following components: single-stranded DNA scaffold (0.01 µM), core staples (0.1 µM), biotin staples (0.01 µM), extended staples for DNA-PAINT (each 1 µM), 1x folding buffer in a total of 50 µl for each sample. Annealing was done by cooling the mixture from 80 °C to 25 °C in 3 hours in a thermocycler. Using a 1:1 ratio between scaffold and biotin staples allows sample

preparation without prior DNA origami purification, where otherwise free biotinylated staples would saturate the streptavidin surface and prevent origami immobilization on the glass surface. As docking strand sequence, we used a 20nt adapter motive[12] (A20: AAGAAAGAAAAGAAGAAAAG), which allowed us to later hybridize any desired docking strand imaging to the origami via a stably-binding complementary adapter 'cA20_DS'. The adapter motive is cA20: CTTTTCTTCTTTTCTTTCTT which is concatenated to the docking strand of choice DS (see **Supplementary Table 2** for sequences).

DNA origami sample preparation. Ibidi 8-well slides were prepared as follows. A 10 µl drop of biotin-labeled bovine albumin (1 mg/ml, dissolved in buffer A) was placed at the chamber center and incubated for 2 min and aspirated. The chamber was then washed with 200 µl of buffer A, aspirated, and then a 10 µl drop streptavidin (0.5 mg/ml, dissolved in buffer A) was placed at the chamber center and incubated for 2 min. After aspirating and washing with 200 µl of buffer A and subsequently with 200 µl of buffer B, a 10 µl of DNA origami (1:100-200 dilution in buffer B from folded stock) was placed at the chamber center and incubated for 5 min. Next, the chamber was washed with 200 µl of Buffer B and docking strand adapters hybridizing to the DNA origami were added at 100 nM in Buffer B, incubated for 5 min and washed with 200 µl Buffer B. Finally, Buffer C and imager strand was added for DNA-PAINT imaging.

Conjugation of antibodies with docking strands. DNA-antibody conjugations were performed in 0.5-mL Amino Ultra Centrifugal Filters with 50 kDa molecular weight cutoffs with DBCO-sulfo-NHS ester cross-linker, which was dissolved at 20 mM DMSO and stored in single-use aliquots at -80° C. This cross-linker links azide-functionalized DNA oligonucleotides to surface-exposed lysine residues. Azide-functionalized DNA oligonucleotides were stored in 1 mM deionized water. Critically, all antibodies were ordered carrier-free, as common preservatives such as bovine serum albumin and sodium azide interfere with the conjugation reaction. First, 500 µL PBS was added to the Amicon filters, which were centrifuged for 5 min at 10,000 rcf. After wetting the filters, 25 µg antibody was added and washed twice with PBS. For each wash, PBS was added to a total volume of 500 µL, and the filters were centrifuged for 5 min at 10,000 rcf. If after the second spin, the total volume remaining in each filter was greater than 100 µL, the filters were centrifuged again for 5 min at 10,000 rcf. After the second PBS wash, a 20-fold molar excess of DBCO-sulfo-NHS ester cross-linker and a 20-fold molar excess of DNA oligonucleotide were added, and after gentle mixing, each conjugation reaction was incubated in the dark at 4° C overnight. The following day, conjugated antibodies were washed three times with PBS, as described above. To elute the antibody, the filter was inverted in a fresh tube and centrifuged for 2 min at 1,500 rcf. The conjugated antibody was transferred to a clean tube, and concentrations were measured using the Qubit Protein Assay. DNA-antibody conjugation was confirmed by comparing unconjugated and conjugated antibodies on NuPage 4-12% Bis-Tris protein gels. For each sample, 0.5 µg total protein was added to NuPage LDS Sample Buffer and 50 mM DTT. Protein was denatured at 80° C for 10 min. Gels were run at 75 V for 5 min, then at 180 V for 60 min. Gels were stained with InstantBlue Coomassie Protein Stain for 15 minutes at room temperature, rinsed with water, and imaged on a Sapphire Biomolecular Imager (Azure Biosystems).

Tissues. Mouse tissue was obtained from naïve control mice meeting experimental endpoint on an approved Harvard Medical School/Longwood Medical Area IACUC protocol.

Cell culture and plating. HeLa cells were maintained in DMEM supplemented with 10% fetal bovine serum at 37 °C with 5% CO_2 and were checked regularly for mycoplasma contamination. For imaging of whole HeLa cells, ~16K cells were seeded in each well of an Ibidi 18-well chamber, placed in the incubator overnight and fixed the following day. For preparation of cell pellets for cryosectioning, ~1 million cells were seeded in 10-cm dishes and placed in the incubator until reaching 70 % confluency.

HeLa cell preparation for cryosectioning. HeLa cells were processed according to previously published protocols[64]. In brief, HeLa cells were grown in 10 cm Petri dishes and once reaching 70 % confluence, were fixed in 4% FA 250 mM HEPES, pH 7.6 for 10 min. Fixative was decanted and cells further fixed with 8% FA in 250 mM HEPES, pH 7.6 for a total of 2h at 4°C. During fixation, cells were gently scraped off the surface unidirectionally using cell scrapers previously soaked in fixative to avoid sticking. Detached cell suspension was transferred into a 1.5 mL hydrophobic Eppendorf tube and centrifuged at increasing speeds to form a pellet of fixed cells: 300 × g, 5 min; 500 × g, 2 min; 1,000 × g, 2 min; 2,000 × g, 2 min; 4,000 × g. At this point, the pellet could be resuspended in 1% FA in 250 mM HEPES, pH 7.6 and stored overnight at 4°C. Next, the pellet was transferred between several drops of 2.1 M sucrose drops to wash away residual fixative and infiltrated 2-4h in 2.1 M sucrose (sucrose acts as cryoprotectant to prevent structural damage during freezing. The pellet becomes transparent). Next, the infiltrated pellet was transferred to a metal pin, residual sucrose carefully removed using filter paper and the pellet shaped into a cone under a dissecting light microscope and using forceps. Finally, the cell pellet was frozen by immersion into liquid nitrogen and was stored indefinitely in liquid nitrogen tanks. We would like to also highlight alternative protocols based on gelatin embedding, which can improve probe handling as discussed in a recent review[33].

Tissue preparation for cryosectioning. Mouse cerebellum and spleen were sectioned into 1-2 mm cubes and incubated consecutively in 4% FA 250 mM HEPES, pH 7.6, in 8% PFA in HEPES for 2 hours at 4°C, and in 1% PFA in HEPES overnight at 4°C. Tissue cubes were then embedded in 7.5% gelatin, 10% Sucrose in PBS (gelatin-sucrose solution was prepared at 70°C and stored in 10mL aliquots at -20°C). Pellets were infiltrated in liquid gelatin-sucrose for 30 minutes at 37°C and subsequently solidified at 4°C. Then, the gel block was removed from the tube, the tissue block cut out as 1mm blocks and transferred into 2.1 M sucrose in PBS for 4h. Lastly, sucrose-infiltrated tissue blocks were placed on metal pins, residual sucrose carefully removed using filter paper, frozen by immersion into liquid nitrogen and stored indefinitely in liquid nitrogen tanks.

Tokuyasu cryosectioning. All Tokuyasu cryosectioning was performed at the Harvard Electron Microscopy Core using a Leica EM UC7 Ultramicrotome equipped with a FC7 cryo-chamber. Frozen cell/tissue samples were cut at a temperature of -110°C and at a ~150 nm section thickness using a diamond knife (Diatome). Lastly, sections were collected using drops a freshly prepared 1:1 mixture of 2.1 M sucrose in PBS and 2% methyl cellulose in water and transferred onto Ibidi 8-well chambers for tokPAINT imaging, that had previously been glow discharged (EMS100x, 2min at 40mA). Sectioned samples can be stored at -20°C for months.

TEM imaging. For transmission electron microscopy imaging, cryosections were placed on formvar-coated grids, washed, and contrasted using methyl cellulose/uranyl acetate. TEM imaging was performed at the Harvard Electron Microscopy Core on a JEOL 1200EX TEM.

Labeling of cryosections for tokPAINT. 8-well chambers containing cryosections were thawed and washed 3× in PBS under agitation for 10min for sucrose removal and quenched with 100mM glycine in 100mM HEPES for 15min. Next, cryosections were permeabilized in 0.3% Triton-X 100 in PBS for 5min, rinsed 3× in PBS and ready for subsequent labeling. Note, that Tokuyasu immunogold protocols vary regarding antibody incubation times. A general rule of thumb is using high antibody concentrations and short incubation times, rather than low concentrations for extended incubations[96]. Hence, we chose relatively high antibody dilutions (1:50-200) and could even observe strong antibody signal for incubations as short as 5min. For a systematic investigation, antibody titration series can be advised. For our proof-of-concept study we applied varying blocking and/or labeling conditions, which are listed in **Supplementary Table 1**

for all experiments with respect to blocking buffer as well as both antibody dilution and incubation times. The blocking buffer was used for both antibody incubations and as a washing solution in between labeling in case of indirect primary and secondary antibody labeling. After antibody incubation, cryosections were washed 3× in PBS, stained with 30 nM DAPI in PBS for 3min and washed again with PBS. Lastly, Buffer C and imager was added for tokPAINT imaging. Note that DAPI staining could faint for several rounds of washing, especially for Exchange-PAINT experiments. However, staining could be simply recovered by performing another round of DAPI staining at the same concentration as stated above. *Phosphatase control (Fig. 2c)*. Two cryosection samples were processed as previously described until the blocking step, at which they were placed for 1h at 37°C and one incubating with alkaline phosphatase to remove phosphorylation site S5p as target antigen[38]. After washing 3× in PBS, normal blocking and indirect immunostaining was performed using a fluorescently-labeled secondary antibody. *Combined a-tubulin and telomere imaging (Fig. 4c)*. Cryosections were labeled for a-tubulin using primary antibody + secondary antibody incubation and postfixed with 4% FA in PBS for 10min followed by a 10min glycine quenching step. Next, the samples were washed with PBS, and incubated with 100-fold diluted RNase A/T1 Mix in 1× PBS at 37 °C for 1 h. Samples were washed 3× in PBS, rinsed and incubated with 50% formamide in 2× SSC for 15min. Next, the sample was placed on a heat block at 90 °C for 4.5 min in 50% formamide in 2× SSC. A 20nt FISH probe against telomeric repeat (AACCCTAACCCTAACCCTAA -A488) was added at 1 µm concentration in 20% formamide, 10% dextran sulfate and 4× SSC and incubated overnight at 37°C for hybridization. Lastly, the sample was washed 2× with 20% formamide 2× SSC, rinsed with PBS, and 30 nM DAPI in PBS for 3min was added. After a final wash in PBS, Buffer C was added and imager for tokPAINT imaging. *mRNA imaging via poly(dT) probes (Fig. 4d)*. Cryosections were treated as described until the blocking step, followed by a 10min wash in 4x SSC. Next, 40nt poly(dT) probe modified with digoxigenin were added in 20% hybridization buffer (20% ethylene carbonate, 10% dextran sulfate and 4× SSC) buffer at 37 °C overnight in a humidity chamber. The next day, the sample was washed 2× with 20% EC 2xSSCT for 15min, followed by three rinses with 4× SSC. The sample was then blocked with 1% gelatin in PBS for 10min and subsequently subject to indirect immunostaining as described in **Supplementary Table 1**. After final washes, Buffer C and imager was added for tokPAINT imaging.

Fixation and labeling of whole HeLa cells. 24h after seeding HeLa cells in Ibidi 18-well chambers, cells were fixed using 4% FA 250 mM HEPES, pH 7.6 for 20min. Next, samples were washed 4× in PBS (30s, 60s, 2×5 min) and both blocked and permeabilized in 3% BSA and 0.25% Triton X-100 in PBS at room temperature for 90 min. Primary rabbit anti-POL II S5p antibody was added at 1:100 in 3% BSA and 0.1% Triton-X 100 in PBS and incubated overnight at 4 °C. The next morning, samples were washed 4x washes in PBS (30s, 60s, 2× 5min) and DNA-conjugated secondary antibody (1:100) was added at 1:100 in 3% BSA and 0.1% Triton-X 100 in PBCS and incubated for 1h at room temperature. Samples were quickly washed 3× in PBS, incubated with gold particles as fiducial markers (1:20 in PBS) for 5 min, washed again 2× in PBS before adding Buffer C and imager for DNA-PAINT imaging.

Super-resolution microscopy setup. TIRF and HILO imaging was carried out at MicRoN Imaging Core at Harvard Medical School on a Nikon Ti inverted microscope equipped with a Nikon Ti-TIRF-EM Motorized Illuminator, a Nikon LUN-F Laser Launch with single fiber output (488nm, 90mW;561 nm, 70mW; 640nm, 65mW) and a Lumencore SpectraX LED Illumination unit. The objective-type TIRF system with an oil-immersion objective (Apo TIRF 100×/1.49 DIC N2). DNA-PAINT experiments were performed using the 560 nm laser line and fluorescence emission was passed through a Chroma ZT 405/488/561/640 multi-band pass dichroic mirror mounted on a Nikon TIRF filter cube located in the filter cube turret and a Chroma ET 595/50m band pass emission filter located on a Sutter emission filter wheel within the infinity space of the stand before image recording on a line on a sCMOS camera (Andor, Zyla 4.2) mounted to a standard Nikon camera port. For astigmatism-based 3D imaging, the C-mount side port of the microscope body was

replaced by a custom-built construction allowing to insert a cylindrical lens in front of the camera (description including component list in **Supplementary Fig. 10**).

Imaging conditions. All fluorescence microscopy data was recorded with the sCMOS camera (2048 × 2048 pixels, pixel size: 6.5 μm). Both microscope and camera were operated with the Nikon Elements software at 2×2 binning and cropped to the center 512 × 512 pixel field-of-view. The camera read out rate was set to 200 MHz and the dynamic range to 16 bit. For detailed imaging parameters specific to the data presented in all main and supplementary figures refer to **Supplementary Table 1**.

Image analysis. Please refer to **Supplementary Fig. 2** and **Supplementary Fig. 4** for a detailed step-by-step illustration through all processing steps of super-resolution reconstruction. All DNA-PAINT/tokPAINT imaging data was processed and reconstructed using the Picasso[9] software suite, Fiji[97,98] and custom, previously-published Python modules[12,99].

Data availability
All data are available in the main text or the supplementary materials, and materials are available upon request.

Code availability
Super-resolution reconstruction was performed using the Picasso[9] suite developed by the Jungmann lab: https://github.com/jungmannlab/picasso. Previously-published custom Python packages employed in this study are available in public repositories: https://github.com/schwille-paint/picasso_addon and https://github.com/schwille-paint/lbFCS2. Additional custom code will be made available via github.com prior to publication.

Acknowledgements

Author contributions

J.S. conceived the study, performed experiments, analyzed data and wrote the manuscript with input from all authors. M.E. performed cryosectioning, provided cryosection samples and performed TEM imaging. M.N. conjugated antibodies, maintained cell culture and provided cell samples for cryoblock preparations. L.M. prepared tissue cryoblocks and performed tissue tokPAINT experiments. S.A. contributed to initial joint experiments and to the manuscript storyline. R.B.M. performed antibody conjugations. L.B. developed code for chromatic aberration correction and contributed to the manuscript storyline. C.P.H. contributed to initial experiments. A.W. and L.A.-J. provided practical training and supported early protocol development J.W. provided helpful advice regarding cryosectioning and TEM data interpretation. P.Y. provided laboratory infrastructure, helpful advice and shared reagents. A.P. hosted a lab visit of J.S., provided training, protocols related to cryosectioning and valuable manuscript input. G.M.C. and C.-t.W. guided the project through joint discussions, valuable feedback and contributed to the manuscript storyline. All authors read and approved the final manuscript.

Competing interests

Potential conflicts of interest for G.M.C. are listed on arep.med.harvard.edu/gmc/tech.html. C.-t.W. holds or has patent filings pertaining to imaging, and her laboratory has held a sponsored research agreement with Bruker Inc. C.-t.W. is a co-founder of Acuity Spatial Genomics and, through personal connections to G.M.C, has equity in companies associated with him, including 10x Genomics and Twist. A.P. holds a patent on 'Genome Architecture Mapping'. P.Y. is also a co-founder, equity holder, director and consultant of Ultivue, Inc. and Digital Biology, Inc. All other authors declare no competing financial interest.

References

1. Klar, T. A., Jakobs, S., Dyba, M., Egner, A. & Hell, S. W. Fluorescence microscopy with diffraction resolution barrier broken by stimulated emission. *Proceedings of the National Academy of Sciences of the United States of America* **97**, 8206–8210 (2000).
2. Betzig, E. *et al.* Imaging Intracellular Fluorescent Proteins at Nanometer Resolution. *Science* **313**, 1642–1645 (2006).
3. Rust, M. J., Bates, M. & Zhuang, X. Sub-diffraction-limit imaging by stochastic optical reconstruction microscopy (STORM). *Nature Methods* **3**, 793 (2006).
4. Sharonov, A. & Hochstrasser, R. M. Wide-field subdiffraction imaging by accumulated binding of diffusing probes. *Proceedings of the National Academy of Sciences* **103**, 18911 LP – 18916 (2006).
5. Huang, B., Bates, M. & Zhuang, X. Super-Resolution Fluorescence Microscopy. *Annual Review of Biochemistry* **78**, 993–1016 (2009).
6. Hell, S. W. *et al.* The 2015 super-resolution microscopy roadmap. *Journal of Physics D: Applied Physics* **48**, 443001 (2015).
7. Lelek, M. *et al.* Single-molecule localization microscopy. *Nature Reviews Methods Primers* **1**, 1–27 (2021).
8. Jungmann, R. *et al.* Single-Molecule Kinetics and Super-Resolution Microscopy by Fluorescence Imaging of Transient Binding on DNA Origami. *Nano Letters* **10**, 4756–4761 (2010).
9. Schnitzbauer, J., Strauss, M. T., Schlichthaerle, T., Schueder, F. & Jungmann, R. Super-resolution microscopy with DNA-PAINT. *Nature Protocols* **12**, 1198 (2017).
10. Strauss, S. *et al.* Modified aptamers enable quantitative sub-10-nm cellular DNA-PAINT imaging. *Nature Methods* **15**, 685–688 (2018).
11. Jungmann, R. *et al.* Quantitative super-resolution imaging with qPAINT. *Nature Methods* **13**, 439 (2016).
12. Stein, J., Stehr, F., Jungmann, R. & Schwille, P. Calibration-free counting of low molecular copy numbers in single DNA-PAINT localization clusters. *Biophysical Reports* **1**, 100032 (2021).
13. Jungmann, R. *et al.* Multiplexed 3D cellular super-resolution imaging with DNA-PAINT and Exchange-PAINT. *Nat Methods* **11**, 313–318 (2014).

14. Schueder, F. *et al.* Multiplexed 3D super-resolution imaging of whole cells using spinning disk confocal microscopy and DNA-PAINT. *Nature Communications* **8**, 2090 (2017).

15. Deschout, H. *et al.* Precisely and accurately localizing single emitters in fluorescence microscopy. *Nature Methods* **11**, 253 (2014).

16. Axelrod, D. Cell-substrate contacts illuminated by total internal reflection fluorescence. *The Journal of Cell Biology* **89**, 141 LP – 145 (1981).

17. Reinhardt, S. C. M. *et al.* Ångström-resolution fluorescence microscopy. *Nature* **617**, 711–716 (2023).

18. Zhao, Z. W. *et al.* Spatial organization of RNA polymerase II inside a mammalian cell nucleus revealed by reflected light-sheet superresolution microscopy. *Proceedings of the National Academy of Sciences* **111**, 681–686 (2014).

19. H Chung, K. K. *et al.* Fluorogenic DNA-PAINT for faster, low-background super-resolution imaging. *Nature Methods* (2022) doi:10.1038/s41592-022-01464-9.

20. Legant, W. R. *et al.* High-density three-dimensional localization microscopy across large volumes. *Nat Methods* **13**, 359–365 (2016).

21. Tokunaga, M., Imamoto, N. & Sakata-Sogawa, K. Highly inclined thin illumination enables clear single-molecule imaging in cells. *Nature Methods* **5**, 159 (2008).

22. Sauer, M. & Heilemann, M. Single-Molecule Localization Microscopy in Eukaryotes. *Chemical Reviews* **117**, 7478–7509 (2017).

23. Nanguneri, S., Flottmann, B., Horstmann, H., Heilemann, M. & Kuner, T. Three-Dimensional, Tomographic Super-Resolution Fluorescence Imaging of Serially Sectioned Thick Samples. *PLOS ONE* **7**, e38098 (2012).

24. Sigal, Y. M., Speer, C. M., Babcock, H. P. & Zhuang, X. Mapping Synaptic Input Fields of Neurons with Super-Resolution Imaging. *Cell* **163**, 493–505 (2015).

25. Klevanski, M. *et al.* Automated highly multiplexed super-resolution imaging of protein nano-architecture in cells and tissues. *Nat Commun* **11**, 1552 (2020).

26. Narayanasamy, K. K. *et al.* Visualizing Synaptic Multi-Protein Patterns of Neuronal Tissue With DNA-Assisted Single-Molecule Localization Microscopy. *Frontiers in Synaptic Neuroscience* **13**, (2021).

27. Narayanasamy, K. K., Rahm, J. V., Tourani, S. & Heilemann, M. Fast DNA-PAINT imaging using a deep neural network. *Nat Commun* **13**, 5047 (2022).

28. Wade, O. K. *et al.* 124-Color Super-resolution Imaging by Engineering DNA-PAINT Blinking Kinetics. *Nano Letters* **19**, 2641–2646 (2019).

29. Banerjee, A., Anand, M., Kalita, S. & Ganji, M. Single-molecule analysis of DNA base-stacking energetics using patterned DNA nanostructures. *Nat. Nanotechnol.* 1–9 (2023) doi:10.1038/s41565-023-01485-1.

30. Peterson, E. M. & Harris, J. M. Identification of Individual Immobilized DNA Molecules by Their Hybridization Kinetics Using Single-Molecule Fluorescence Imaging. *Analytical Chemistry* **90**, 5007–5014 (2018).

31. Bauer, J., Reichl, A. & Tinnefeld, P. Kinetic Referencing Allows Identification of Epigenetic Cytosine Modifications by Single-Molecule Hybridization Kinetics and Superresolution DNA-PAINT Microscopy. *ACS Nano* (2023) doi:10.1021/acsnano.3c08451.

32. Tokuyasu, K. T. A TECHNIQUE FOR ULTRACRYOTOMY OF CELL SUSPENSIONS AND TISSUES. *Journal of Cell Biology* **57**, 551–565 (1973).

33. Möbius, W. & Posthuma, G. Sugar and ice: Immunoelectron microscopy using cryosections according to the Tokuyasu method. *Tissue and Cell* **57**, 90–102 (2019).

34. Geertsema, H. J. *et al.* Left-handed DNA-PAINT for improved super-resolution imaging in the nucleus. *Nature Biotechnology* 1–4 (2021) doi:10.1038/s41587-020-00753-y.

35. Misteli, T. The Self-Organizing Genome: Principles of Genome Architecture and Function. *Cell* **183**, 28–45 (2020).

36. Pombo, A. & Dillon, N. Three-dimensional genome architecture: Players and mechanisms. *Nature Reviews Molecular Cell Biology* **16**, 245–257 (2015).

37. Guillot, P. V., Xie, S. Q., Hollinshead, M. & Pombo, A. Fixation-induced redistribution of hyperphosphorylated RNA polymerase II in the nucleus of human cells. *Experimental Cell Research* **295**, 460–468 (2004).

38. Xie, S. Q., Martin, S., Guillot, P. V., Bentley, D. L. & Pombo, A. Splicing Speckles Are Not Reservoirs of RNA Polymerase II, but Contain an Inactive Form, Phosphorylated on Serine2 Residues of the C-Terminal Domain. *Molecular Biology of the Cell* **17**, (2006).

39. Branco, M. R. & Pombo, A. Intermingling of Chromosome Territories in Interphase Suggests Role in Translocations and Transcription-Dependent Associations. *PLOS Biology* **4**, e138 (2006).

40. Thevathasan, J. V. *et al.* Nuclear pores as versatile reference standards for quantitative superresolution microscopy. *Nature Methods* **16**, 1045–1053 (2019).

41. Gunasekara, H. *et al.* Superresolution Imaging with Single-Antibody Labeling. *Bioconjugate Chem.* **34**, 825–833 (2023).

42. Unterauer, E. M. *et al.* Spatial proteomics in neurons at single-protein resolution. 2023.05.17.541210 Preprint at https://doi.org/10.1101/2023.05.17.541210 (2023).

43. Gwosch, K. C. *et al.* MINFLUX nanoscopy delivers 3D multicolor nanometer resolution in cells. *Nature Methods* **17**, 217–224 (2020).

44. Bates, M. *et al.* Optimal precision and accuracy in 4Pi-STORM using dynamic spline PSF models. *Nat Methods* **19**, 603–612 (2022).

45. Clowsley, A. H. *et al.* Repeat DNA-PAINT suppresses background and non-specific signals in optical nanoscopy. *Nature Communications* **12**, 1–10 (2021).

46. Otterstrom, J. *et al.* Super-resolution microscopy reveals how histone tail acetylation affects DNA compaction within nucleosomes in vivo. *Nucleic acids research* **47**, 8470–8484 (2019).

47. Frottin, F. *et al.* The nucleolus functions as a phase-separated protein quality control compartment. *Science* **365**, 342–347 (2019).

48. Castells-Garcia, A. *et al.* Super resolution microscopy reveals how elongating RNA polymerase II and nascent RNA interact with nucleosome clutches. *Nucleic Acids Research* **50**, 175–190 (2022).

49. Sasaki, H. M., Kishi, J. Y., Wu, C., Beliveau, B. J. & Yin, P. Quantitative multiplexed imaging of chromatin ultrastructure with Decode-PAINT. *bioRxiv* 2022.08.01.502089 (2022) doi:10.1101/2022.08.01.502089.

50. Kimura, H. & Sato, Y. Imaging transcription elongation dynamics by new technologies unveils the organization of initiation and elongation in transcription factories. *Current Opinion in Cell Biology* **74**, 71–79 (2022).

51. Niederauer, C. *et al.* Direct characterization of the evanescent field in objective-type total internal reflection fluorescence microscopy. *Optics Express* **26**, 20492–20506 (2018).

52. Endesfelder, U., Malkusch, S., Fricke, F. & Heilemann, M. A simple method to estimate the average localization precision of a single-molecule localization microscopy experiment. *Histochemistry and Cell Biology* **141**, 629–638 (2014).

53. Rothemund, P. W. K. Folding DNA to create nanoscale shapes and patterns. *Nature* **440**, 297 (2006).

54. Ester, M., Kriegel, H.-P., Sander, J. & Xu, X. A Density-Based Algorithm for Discovering Clusters in Large Spatial Databases with Noise. *Proceedings of the 2nd International Conference on Knowledge Discovery and Data Mining* 226–231 (1996).

55. Stein, J. *et al.* Toward Absolute Molecular Numbers in DNA-PAINT. *Nano Letters* **19**, 8182–8190 (2019).

56. Schueder, F. *et al.* Unraveling cellular complexity with unlimited multiplexed super-resolution imaging. 2023.05.17.541061 Preprint at https://doi.org/10.1101/2023.05.17.541061 (2023).

57. Liu, S., Hoess, P. & Ries, J. Super-Resolution Microscopy for Structural Cell Biology. *Annual Review of Biophysics* **51**, 301–326 (2022).

58. Blumhardt, P. *et al.* Photo-Induced Depletion of Binding Sites in DNA-PAINT Microscopy. *Molecules* **23**, 3165 (2018).

59. Pombo, A. *et al.* Regional specialization in human nuclei: visualization of discrete sites of transcription by RNA polymerase III. *The EMBO Journal* **18**, 2241–2253 (1999).

60. Kimura, H., Tao, Y., Roeder, R. G. & Cook, P. R. Quantitation of RNA Polymerase II and Its Transcription Factors in an HeLa Cell: Little Soluble Holoenzyme but Significant Amounts of Polymerases Attached to the Nuclear Substructure. *Molecular and Cellular Biology* **19**, 5383–5392 (1999).

61. Kim, J., Venkata, N. C., Hernandez Gonzalez, G. A., Khanna, N. & Belmont, A. S. Gene expression amplification by nuclear speckle association. *Journal of Cell Biology* **219**, e201904046 (2019).

62. Sograte-Idrissi, S. *et al.* Nanobody Detection of Standard Fluorescent Proteins Enables Multi-Target DNA-PAINT with High Resolution and Minimal Displacement Errors. *Cells* **8**, 48 (2019).

63. Götzke, H. *et al.* The ALFA-tag is a highly versatile tool for nanobody-based bioscience applications. *Nat Commun* **10**, 4403 (2019).

64. Xie, S. Q., Lavitas, L. M. & Pombo, A. CryoFISH: fluorescence in situ hybridization on ultrathin cryosections. *Methods in molecular biology (Clifton, N.J.)* **659**, 219–230 (2010).

65. Ilik, İ. A. *et al.* SON and SRRM2 are essential for nuclear speckle formation. *eLife* **9**, e60579 (2020).

66. Dechat, T. *et al.* Nuclear lamins: major factors in the structural organization and function of the nucleus and chromatin. *Genes Dev.* **22**, 832–853 (2008).

67. Ikegami, K., Secchia, S., Almakki, O., Lieb, J. D. & Moskowitz, I. P. Phosphorylated Lamin A/C in the Nuclear Interior Binds Active Enhancers Associated with Abnormal Transcription in Progeria. *Developmental Cell* **52**, 699-713.e11 (2020).

68. Chen, Y. *et al.* Mapping 3D genome organization relative to nuclear compartments using TSA-Seq as a cytological ruler. *Journal of Cell Biology* **217**, 4025–4048 (2018).

69. Ferrai, C. *et al.* Poised Transcription Factories Prime Silent uPA Gene Prior to Activation. *PLOS Biology* **8**, e1000270 (2010).

70. Huang, B., Wang, W., Bates, M. & Zhuang, X. Three-Dimensional Super-Resolution Imaging by Stochastic Optical Reconstruction Microscopy. *Science* **319**, 810813 (2008).

71. Franke, C. *et al.* Approach to map nanotopography of cell surface receptors. *Commun Biol* **5**, 1–16 (2022).

72. Stierhof, Y.-D., Schwarz, H. & Frank, H. Transverse sectioning of plastic-embedded immunolabeled cryosections: Morphology and permeability to protein A-colloidal gold complexes. *Journal of Ultrastructure and Molecular Structure Research* **97**, 187–196 (1986).

73. Balzarotti, F. *et al.* Nanometer resolution imaging and tracking of fluorescent molecules with minimal photon fluxes. *Science* **355**, 606–612 (2017).

74. Ostersehlt, L. M. *et al.* DNA-PAINT MINFLUX nanoscopy. *Nature Methods 2022* 1–4 (2022) doi:10.1038/s41592-022-01577-1.

75. Li, Y. *et al.* Real-time 3D single-molecule localization using experimental point spread functions. *Nature Methods* **15**, 367 (2018).

76. Fu, S. *et al.* Field-dependent deep learning enables high-throughput whole-cell 3D super-resolution imaging. *Nat Methods* **20**, 459–468 (2023).

77. Thiele, J. C. *et al.* Isotropic three-dimensional dual-color super-resolution microscopy with metal-induced energy transfer. *Science Advances* **8**, eabo2506 (2022).

78. Huang, F. *et al.* Ultra-High Resolution 3D Imaging of Whole Cells. *Cell* **166**, 1028–1040 (2016).

79. Shtengel, G. *et al.* Interferometric fluorescent super-resolution microscopy resolves 3D cellular ultrastructure. *Proceedings of the National Academy of Sciences* **106**, 3125–3130 (2009).

80. Strauss, S. & Jungmann, R. Up to 100-fold speed-up and multiplexing in optimized DNA-PAINT. *Nature Methods* **17**, 1–3 (2020).

81. Vicidomini, G. *et al.* High Data Output and Automated 3D Correlative Light–Electron Microscopy Method. *Traffic* **9**, 1828–1838 (2008).

82. Micheva, K. D. & Smith, S. J. Array Tomography: A New Tool for Imaging the Molecular Architecture and Ultrastructure of Neural Circuits. *Neuron* **55**, 25–36 (2007).

83. Ricci, M. A., Manzo, C., García-Parajo, M. F., Lakadamyali, M. & Cosma, M. P. Chromatin Fibers Are Formed by Heterogeneous Groups of Nucleosomes In Vivo. *Cell* **160**, 1145–1158 (2015).

84. Marenda, M., Lazarova, E., van de Linde, S., Gilbert, N. & Michieletto, D. Parameter-free molecular super-structures quantification in single-molecule localization microscopy. *Journal of Cell Biology* **220**, e202010003 (2021).

85. Gómez-García, P. A. *et al.* Mesoscale Modeling and Single-Nucleosome Tracking Reveal Remodeling of Clutch Folding and Dynamics in Stem Cell Differentiation. *Cell Reports* **34**, 108614 (2021).

86. Irgen-Gioro, S., Yoshida, S., Walling, V. & Chong, S. Fixation can change the appearance of phase separation in living cells. *eLife* **11**, e79903 (2022).

87. van Donselaar, E., Posthuma, G., Zeuschner, D., Humbel, B. M. & Slot, J. W. Immunogold Labeling of Cryosections from High-Pressure Frozen Cells. *Traffic* **8**, 471–485 (2007).

88. D'Este, E., Lukinavičius, G., Lincoln, R., Opazo, F. & Fornasiero, E. F. Advancing cell biology with nanoscale fluorescence imaging: essential practical considerations. *Trends in Cell Biology* **0**, (2024).

89. Kopek, B. G. *et al.* Diverse protocols for correlative super-resolution fluorescence imaging and electron microscopy of chemically fixed samples. *Nat Protoc* **12**, 916–946 (2017).

90. van Elsland, D. M. *et al.* Ultrastructural Imaging of Salmonella–Host Interactions Using Super-resolution Correlative Light-Electron Microscopy of Bioorthogonal Pathogens. *ChemBioChem* **19**, 1766–1770 (2018).

91.   Franke, C. *et al.* Correlative single-molecule localization microscopy and electron tomography reveals endosome nanoscale domains. *Traffic* **20**, 601–617 (2019).

92.   van der Beek, J., de Heus, C., Liv, N. & Klumperman, J. Quantitative correlative microscopy reveals the ultrastructural distribution of endogenous endosomal proteins. *Journal of Cell Biology* **221**, e202106044 (2021).

93.   Truckenbrodt, S. Expansion Microscopy: Super-Resolution Imaging with Hydrogels. *Anal. Chem.* **95**, 3–32 (2023).

94.   Hamel, V. & Guichard, P. Chapter 14 - Improving the resolution of fluorescence nanoscopy using post-expansion labeling microscopy. in *Methods in Cell Biology* (eds. Guichard, P. & Hamel, V.) vol. 161 297–315 (Academic Press, 2021).

95.   Stehr, F., Stein, J., Schueder, F., Schwille, P. & Jungmann, R. Flat-top TIRF illumination boosts DNA-PAINT imaging and quantification. *Nature Communications* **10**, 1268 (2019).

96.   Griffiths, G. *Fine Structure Immunocytochemistry*. (Springer Berlin Heidelberg, Berlin, Heidelberg, 1993). doi:10.1007/978-3-642-77095-1.

97.   Schindelin, J. *et al.* Fiji: an open-source platform for biological-image analysis. *Nat Methods* **9**, 676–682 (2012).

98.   Preibisch, S., Saalfeld, S., Schindelin, J. & Tomancak, P. Software for bead-based registration of selective plane illumination microscopy data. *Nat Methods* **7**, 418–419 (2010).

99.   Stehr, F. *et al.* Tracking single particles for hours via continuous DNA-mediated fluorophore exchange. *Nature Communications 2021 12:1* **12**, 1–8 (2021).